

RESEARCH ARTICLE

10.1029/2018JD028438

Key Points:

- The long record of satellite-measured CO from MOPITT enables study of interannual variability (IAV)
- ENSO climate mode index is important, but we find that other modes are also required to predict CO IAV
- Interaction of climate modes is necessary to explain CO variability

Supporting Information:

- Supporting Information S1

Correspondence to:

R. R. Buchholz,
buchholz@ucar.edu

Citation:

Buchholz, R. R., Hammerling, D., Worden, H. M., Deeter, M. N., Emmons, L. K., Edwards, D. P., & Monks, S. A. (2018). Links between carbon monoxide and climate indices for the Southern Hemisphere and tropical fire regions. *Journal of Geophysical Research: Atmospheres*, 123, 9786–9800. <https://doi.org/10.1029/2018JD028438>

Received 30 JAN 2018

Accepted 1 JUL 2018








Accepted article online 18 JUL 2018

Published online 4 SEP 2018

Corrected 17 SEP 2018

This article was corrected on 17 SEP 2018. See the end of the full text for details.

Links Between Carbon Monoxide and Climate Indices for the Southern Hemisphere and Tropical Fire Regions

R. R. Buchholz¹ , D. Hammerling² , H. M. Worden¹ , M. N. Deeter¹ , L. K. Emmons¹ , D. P. Edwards¹ , and S. A. Monks³ 

¹Atmospheric Chemistry Observations & Modeling Laboratory, National Center for Atmospheric Research, Boulder, CO, USA, ²Computational and Information Systems Laboratory, National Center for Atmospheric Research, Boulder, CO, USA, ³Earth System Research Laboratory, National Oceanic and Atmospheric Administration, Boulder, CO, USA

Abstract In the Southern Hemisphere and tropics, the main contribution to carbon monoxide (CO) variability is from fire emissions, which are connected to climate through the availability, type, and dryness of fuel. Here we assess the data-driven relationships between CO and climate, aiming to predict atmospheric loading during fire seasons. Observations of total column CO from the Measurements Of Pollution In The Troposphere satellite instrument are used to build a record of monthly anomalies between 2001 and 2016, focusing on seven biomass burning regions of the Southern Hemisphere and tropics. With the exception of 2015, the range of absolute variability in CO is similar between regions. We model CO anomalies in each of the regions using climate indices for the climate modes: El Niño–Southern Oscillation, Indian Ocean Dipole, Tropical South Atlantic, and Antarctic Oscillation. Stepwise forward and backward variable selection is used to choose from statistical regression models that use combinations of climate indices, at lag times between 1 and 8 months relative to CO anomalies. The Bayesian information criterion selects models with the best predictive power. We find that all climate mode indices are required to model CO in each region, generally explaining over 50% of the variability and over 70% for tropical regions. First-order interaction terms of the climate modes are necessary, producing greatly improved explanation of CO variability over single terms. Predictive capability is assessed for the Maritime Southeast Asia and the predicted peak CO anomaly in 2015 is within 20% of the measurements.

1. Introduction

The link between fire and atmospheric carbon monoxide (CO) is well established for the Southern Hemisphere and tropics (e.g., Edwards, Emmons, et al., 2006; Gloude-mans et al., 2006). In the Southern Hemisphere, biomass burning is the main source of CO variability (e.g., Voulgarakis et al., 2015). Atmospheric CO is produced directly by incomplete combustion from biomass burning as well as fossil fuel use and indirectly by photochemistry. In addition to being a criteria pollutant that degrades air quality, CO plays a critical role in tropospheric chemistry as a precursor to ozone (O₃) and as a primary sink for the hydroxyl radical (OH). CO has a moderate lifetime of weeks to months, making observations of CO from space useful for tracking committed pollutants that are more difficult to measure, such as black carbon (Arellano et al., 2010) and other aerosols and trace gases (Bian et al., 2010; Edwards et al., 2004; Pumphrey et al., 2011; Zhang et al., 2006). Predictions of CO loading can therefore serve as a proxy for other air pollutants, such as aerosols, in air quality forecasts during fire seasons.

While ignition of fires in the present era is predominantly due to humans (Bowman et al., 2011; Costafreda-Aumedes et al., 2017), fire intensity and burned area are related to the amount, type, and dryness of available fuel, which respond to climate-driven water availability combined with ecosystem responses (van der Werf et al., 2008). Consequently, the magnitude of emissions from biomass burning, such as for CO, is connected to climate variability. Emissions of CO contribute to air pollution near fire sources, as well as globally through long-range transport. Although emissions are the main driver in the regions we study (Voulgarakis et al., 2010, 2015), transport patterns can also contribute to CO variability (e.g., Bowman, 2006). Therefore, climate influences on both emissions and dynamics can play a role in determining CO interannual variability (IAV).

Relationships between climate conditions and fire occurrence have been previously studied. For instance, fire responds differently to rainfall depending on the region of interest. Drought was found to increase fire occurrence in Maritime SEA (Andela & van der Werf, 2014; van der Werf et al., 2008) and exponentially increase resulting emissions (Yin et al., 2016) due to more agricultural burning of drained swampland that introduced high CO-emitting peat to fire (Field et al., 2016). In contrast, drought reduced fire frequency in Australia, while fire relationships to rainfall in Africa and South America are spatially varying, depending on the balance between rainfall's influence on growth of available fuel and the length of the dry season (Andela & van der Werf, 2014; Aragão et al., 2007; van der Werf et al., 2008). Bloom et al. (2015) suggested that large differences in fire emissions between 2 years with similar total burnt area in South America were due to reduced vegetation growth impacted by drought.

The El Niño–Southern Oscillation (ENSO) climate mode is often used as a prediction of regional climate variability. However, other climate modes have been linked to teleconnections with regional climate responses, such as influencing rainfall and drought (e.g., Andreoli & Kayano, 2006; Hendon et al., 2007; Marengo et al., 2016; Saji & Yamagata, 2003). Impacting regional climate has the potential to influence biomass burning. For example, Field et al. (2009) found that the Indian Ocean Dipole (IOD) was just as important a contributor as ENSO to fires in Indonesia. The direct influence of multiple climate modes on fires was investigated by Chen et al. (2016), who used a set of ocean climate indices to model global burned area using multilinear regression and found that a combination of two climate modes describes more variability in burned area than a single climate mode. Additionally, the interaction of climate modes is important. For instance, Cleverly et al. (2016) found that interacting climate modes were responsible for the Australian water and carbon sink in 2011. Furthermore, they found that when IOD and ENSO modes are synchronized, the impact on rainfall was substantially larger than when not synchronized.

In contrast to fire products and emissions, limited research has linked atmospheric CO loading variability with climate modes. Edwards, Pétron, et al. (2006) used 5 years of CO retrievals from the Measurements Of Pollution In The Troposphere (MOPITT) satellite instrument. They suggested a connection between ENSO, burned area, and CO anomalies for four regions of the Southern Hemisphere and tropics. Here we extend the analysis of Edwards, Pétron, et al. (2006) to include MOPITT data up to 2016 and examine links between CO and multiple climate modes, including ENSO. We follow a similar method to Wespes et al. (2016, 2017), who develop relationships between atmospheric composition (O_3 loading) and a range of descriptive variables, including climate modes. Our focus is on the relationship between four climate modes and CO IAV and to assess the importance of climate mode interactions.

The satellite data set, regions of interest, and climate indices are outlined in section 2. Section 3 discusses CO variability in the selected regions of the Southern Hemisphere and tropics. We systematically develop explanatory models between climate mode indices and CO IAV, with the goal of predicting future CO loading. Statistical methodology and resulting models with the most predictive power are presented in section 4, and model predictive capability for the Maritime SEA region is assessed in section 4.3. Potential causal implications are discussed in section 5, and section 6 presents our conclusions.

2. Observational Data Sets

2.1. Satellite Observations

The MOPITT instrument on the National Aeronautics and Space Administration Earth Observing System/Terra satellite provides the longest record of CO measurements from space, currently with over 18 years of near-continuous data, starting in 2000. Equator overpass occurs at $\sim 10:30$ and $\sim 22:30$ (local solar time), and MOPITT uses a cross-track scan that allows for complete Earth coverage in about 3 days, with a ground-pixel size of 22×22 km. Extensive validation studies cover a wide variety of locations and environments (e.g., Buchholz et al., 2017; Deeter et al., 2017; Emmons et al., 2009).

MOPITT retrievals use the optimal estimation retrieval approach (Deeter et al., 2003; Rodgers, 2000). A priori profiles are combined with radiance measurements to statistically determine a maximum a posteriori solution. We use MOPITT version 7 (V7), which has a priori profiles gridded at 1.9° latitude \times 2.5° longitude resolution, taken from a climatological 2000–2009 run of CAM-chem (Lamarque et al., 2012). MOPITT retrievals use the MERRA reanalysis products (Modern-Era Retrospective analysis for Research Applications) to estimate meteorological parameters in the retrieval process (Rienecker et al., 2011). Major improvements in the V7 product

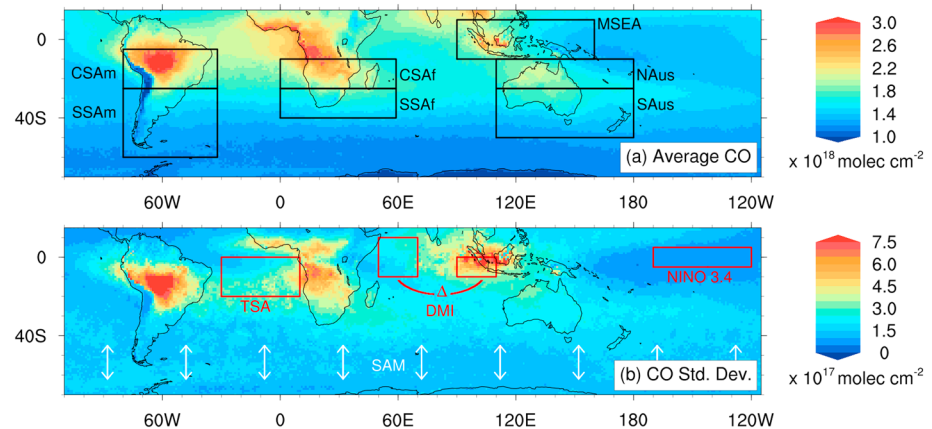


Figure 1. Boxes in (a) define the regions of interest and are overplotted on a map of average September to December total column CO from Measurements of Pollution in the Troposphere V7-thermal infrared between 2001 and 2016. Note that we select only retrievals over land within these boundaries. MSEA = Maritime SEA; NAus = North Australasia; SAus = South Australasia; CSAf = Central Southern Africa; SSAf = South Southern Africa; CSAm = Central South America; SSAm = Southern South America. The base plot in (b) is standard deviation of total column CO that corresponds to (a), overplotted in red boxes that define regions of the sea surface temperature climate indices, TSA, DMI, and Niño3.4. White arrows schematically depict the displacement of westerly winds associated with the atmospherically defined climate index, SAM. Climate indices are described in section 2.2. TSA = Tropical South Atlantic; DMI = Dipole Mode Index; SAM = Southern Annular Mode.

are described in Deeter et al. (2017). MOPITT products are publicly available through several repositories linked via <http://terra.nasa.gov/about/terra-instruments/mopitt> or <https://www2.acom.ucar.edu/mopitt>.

The stable systematic bias found for the MOPITT total column product makes it well suited for analyzing long time series (Deeter et al., 2017). In order to reduce systematic and random error, we select daytime, land-only retrievals from the thermal infrared (TIR) product (MOPITT Science Team, 2013). Daytime retrievals have higher sensitivity to CO due to higher thermal contrast compared with nighttime retrievals (Deeter et al., 2007). Restricting analysis to land-only scenes minimizes the effect of different retrieval sensitivity between land and water scenes. The TIR product has lower random error compared to the near-infrared or multispectral products (Deeter et al., 2014) and similar sensitivity as the multispectral product to total column CO from large-scale fires. Averaging over large areas and month time scales further reduces random error to negligible amounts. We find that spatial averages over large areas, such as the regions chosen in this study, produce equivalent CO timeseries and anomalies for TIR and multispectral products (not shown). Therefore, while we only analyze the TIR product, results will translate to the multispectral product.

For each region of interest, a spatial and climatological average of monthly total column CO between 2001 and 2016 is determined and subtracted from monthly average values to produce a time series of monthly CO anomalies. The anomaly data sets developed and used in this study are publicly available through the National Center for Atmospheric Research (NCAR) Research Data Archive (<https://rda.ucar.edu/datasets/ds682.0>, doi: 10.5065/D61N7ZX4).

2.1.1. Selected Regions

We investigate IAV in CO for four main biomass burning regions in the tropics and Southern Hemisphere: Maritime SEA (10–10°N, 90–160°E), Australasia (50–10°S, 110–180°E), southern Africa (40–10°S, 0–60°E) and South America (60–5°S, 80–32°W; Figure 1). The latter three regions required splitting into subregions in order to account for different CO variability patterns within each subregion. In general, we split these regions into tropical and temperate regions at 25°S. While the tropical regions tend to have more biomass burning than the temperate ones, temperate regions are more populated and air quality has a greater potential for impacts on human health.

Australasia is split into two regions, approximately into tropical (North Australasia: 25–10°S, 110–180°E) and temperate (South Australasia: 50–25°S, 110–180°E) subregions. The frequency of large fires is substantially higher in the tropical subregion compared to the temperate subregion (Russell-Smith et al., 2007), and peak fire seasons differ between the subregions (Langmann et al., 2009; Russell-Smith et al., 2007). Additionally, the majority of agricultural activities are found below 25°S (Bryan et al., 2016) as well as more than 85%

Table 1
Overview of Climate Mode Indices Used in This Study

Climate mode	Index name	Source
ENSO	Niño 3.4	www.cpc.ncep.noaa.gov/data/indices/
IOD	Dipole Mode Index (DMI)	stateofocean.osmc.noaa.gov/sur/ind/dmi.php
TSA	Tropical South Atlantic (TSA)	www.cpc.ncep.noaa.gov/data/indices/
AAO	Southern Annular Mode (SAM)	www.cpc.ncep.noaa.gov/products/precip/CWlink/daily_ao_index/ao/ao.shtml

Note. ENSO = El Niño–Southern Oscillation; IOD = Indian Ocean Dipole; TSA = Tropical South Atlantic; AAO = Antarctic Oscillation.

of the Australasia human population (Australian Bureau of Statistics, 2016). The standard deviation in CO (Figure 1b) supports a split at 25°S, indicating higher standard deviation in the tropical region compared to the temperate region.

Two regions in southern Africa are investigated (Central Southern Africa: 25–10°S, 0–60°E, South Southern Africa: 40–25°S, 0–60°E) because they produce clear signals in CO variability. They were split based on burned area trends (Andela & van der Werf, 2014) and the peak fire season (Langmann et al., 2009). We initially considered a third latitudinally defined region (between 10°S and 5°N), but sources of atmospheric CO here are a combination of competing patterns only partially responsive to climate-driven biomass burning. These sources include anthropogenic and biogenic CO, mixing from the Northern Hemisphere as well as seasonally variable biomass burning, resulting in unclear patterns of overall CO variability and consequently discounting this region from further study.

We analyze two regions in South America, split into north and south at 25°S and excluding areas north of 5°S because of multiple competing influences. Enhanced deforestation occurs in the northern tropical region (Central South America: 25–5°S, 83–32°W) compared to the southern region (Southern South America: 58–25°S, 80–32°W), with peak deforestation occurring in the *arc of deforestation* (Aragão & Shimabukuro, 2010; Davidson et al., 2012). Although Chen et al. (2016) found different influences on burned area in the east and west of the tropical region, prevailing easterly winds will tend to correlate CO variability between the east and west; therefore, we retain one whole tropical region.

2.2. Climate Indices

Climate modes are chosen based on representing variability in dynamical processes for the major ocean basins of the Southern Hemisphere and tropics. These modes are linked to regional climate responses such as rainfall, and as a result we expect a relationship with drought, fires, and consequently CO anomalies. We use measurement-based month average indices for climate modes over four ocean regions (Figure 1b): ENSO represents the Pacific Ocean, IOD covers the Indian Ocean, the Tropical South Atlantic (TSA) for the southern Atlantic Ocean, and the Antarctic Oscillation (AAO) for the Southern Ocean. Indices for each of these modes are summarized in Table 1, and data sets are publicly available from either the Climate Prediction Center or State of the Ocean repositories, which are both managed by the National Oceanic and Atmospheric Administration (NOAA).

Indices for ENSO (Niño 3.4; Bamston et al., 1997) and TSA (Enfield et al., 1999) are calculated using sea surface temperature (SST) anomalies in the regions 170–120°W, 5–5°N, and 30–10°E, 20–0°S, respectively. The IOD index is calculated using SST gradients between two regions 50–70°E, 10–10°N, and 90–110°E, 10–0° (DMI, Saji et al., 1999). SST indices are created from the global Optimum Interpolation analysis: Reynolds Olv2 SST (Reynolds et al., 2002), which is calculated using in situ and satellite measurements combined with simulations of SST in sea ice regions. Satellite data are adjusted for biases prior to SST data set calculation (Reynolds, 1988; Reynolds & Marsico, 1993).

The normalized index for AAO (SAM) captures Antarctic atmospheric circulation variability and describes the poleward shift of westerly winds relative to the South Pole (e.g., Thompson & Wallace, 2000). The AAO index is calculated by projecting observational height anomalies at 700 hPa and poleward of 20°S onto the leading empirical orthogonal function of the National Centers for Environmental Prediction/NCAR reanalysis, which is determined over the base period of 1979 to 2000 (Kalnay et al., 1996; Kistler et al., 2001).

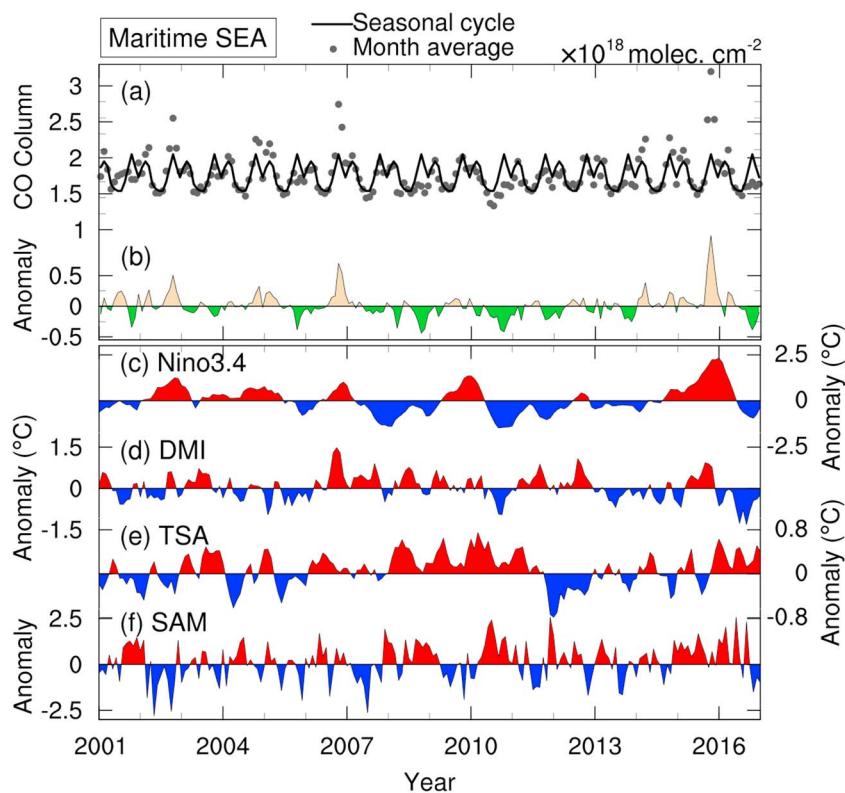


Figure 2. Maritime SEA time series, 2001 to 2016, of (a) month average CO (gray circles) with the climatological seasonal cycle (black line), (b) CO anomalies showing positive anomalies in tan and negative anomalies in green, and (c–f) climate indices over the dates of interest with positive modes in red and negative modes in blue. SEA = Southeast Asia; DMI = Dipole Mode Index; TSA = Tropical South Atlantic; SAM = Southern Annular Mode.

3. IAV in CO

In every region of interest, the average CO seasonal cycle displays a peak associated with biomass burning season, between September and October, reflecting the impact of local and/or transported emissions (Figure 2a and supporting information Figures S2a, S2c, S3a, S3c, S4a, and S4c). Generally, only one annual maximum is present, with the exception of the Maritime SEA region, which shows a smaller secondary peak in March. This is most likely due to transport of fire emissions during the upper ASEAN (Association of Southeast Asian Nations) countries' peak biomass burning season, which lasts from January–April (Bhardwaj et al., 2016; Edwards, Pétron, et al., 2006). We do not consider this secondary peak in our study.

Anomalies in CO are calculated by subtracting climatological seasonal cycle from month average values and are shown in Figure 2b and lower panels of supporting information Figures S2, S3, and S4. These anomalies are much larger than random error, which is on the order of the zero-linewidth in Figure 2b. Anomalies clearly indicate the regional IAV in CO loading over the 2001 to 2016 time period. In all regions, a higher frequency of negative CO anomalies were present between 2008 and 2014 than outside those times. This potentially reflects the global downward trend in CO (Worden et al., 2013). For the Maritime SEA region, the magnitude of positive anomalies is enhanced in the later record relative to the early record, potentially indicating a general upward trend in emissions for this region due to a general overall increase in biomass burning since 2000 (Fanin & van der Werf, 2017; Jiang et al., 2017; Stavrou et al., 2014), which is not observed in the other regions. However, we find a lack of trend significance, which is further discussed in section 4.2.

North Australasia shows higher variability than South Australasia, due to uncontrolled northern Savannah fires, compared to fires in the south where human intervention is easier and more pertinent due to higher populations (Russell-Smith et al., 2007). Central Southern Africa shows more dispersed peak of signal than Southern South Africa, which may be due to multiple vegetation types within the central region combined with the influence of annually varying transport of Northern Hemisphere pollution. The central region of South America experiences variable human influence from burning in the arc of deforestation and

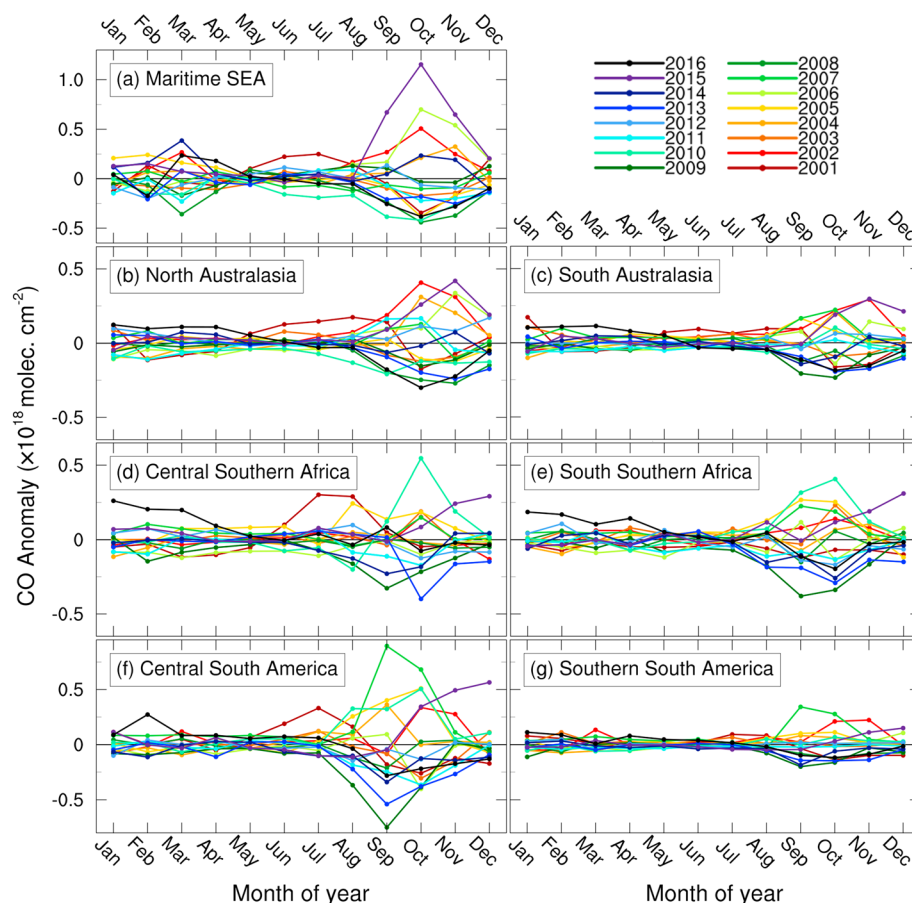


Figure 3. Variability in monthly atmospheric CO after subtraction of mean monthly values, plotted for multiple years for different regions. Different years are represented by different colors.

consequently sees larger IAV in CO compared to the southern region. There is also a recent decrease in the magnitude of positive anomalies over South America (supporting information Figure S4) that could be a response to a slow down in deforestation on the continent, mainly in Brazil (Austin et al., 2017; Jiang et al., 2017; Reddington et al., 2015).

In order to investigate the variability in CO further, we overplot the annual cycle of anomalies (Figure 3). This shows that the largest and most variable deviations from the mean seasonal cycle occur during the biomass burning season. Similar to the climatological seasonal cycle, regions show one period of peak variability, apart from Maritime SEA that also includes enhanced variability during March. Discounting the influence of the large El Niño that occurred in 2015, all regions generally show a range of anomalies within $\pm 5 \times 10^{17}$ molecules cm^{-2} , which represents a range of approximately $\pm 25\%$, relative to the climatological month average values for each region. Although Edwards, Pétron, et al. (2006) showed that for the beginning of the record, Maritime SEA and Australasia exhibited the highest variability, the longer record indicates that variability in anomalies is similar between regions, with tropical regions generally showing higher variability than equivalent temperate regions. Additionally, the largest anomalies occur in different years for different regions.

Since fire is the major driver of CO IAV in these regions, and fire landscape responses are driven by climate, we investigate links between climate variability and atmospheric CO loading. The climate variability in the four major ocean basins relevant for this study is represented by climate indices (defined in section 2.2), which are displayed in Figures 2c–2f. The positive phase of ENSO (El Niño) is generally associated with positive CO anomalies. Edwards, Pétron, et al. (2006) noted this relationship for the MOPITT record between 2000 and 2005 and linked enhanced CO in El Niño years to increased fire activity. The first 5 years in Figure 2 suggests an intensity-based relationship, with higher MOPITT CO enhancements in larger El Niño years.

However, when interpreting the 16-year record, the relationship between CO and ENSO is more complicated. For instance, the 2009/2010 El Niño was larger than in 2006/2007 but induced lower CO anomalies in Maritime SEA and South America. In the South America region, Bloom et al. (2015) found similar burnt area during these two El Niño events but different combustion efficiency, which they attributed to different plant productivity impacted by regional drought. A similar variable relationship between ENSO and CO anomalies is observed in the other regions.

We perform single-variable lagged correlation analysis between each climate index and regional CO anomalies and find that the climate indices show maximum correlation at various time lags depending on the index (supporting information Figure S1). Also, correlation with indices other than ENSO in some regions is equal or larger in magnitude than the correlation with ENSO (e.g., DMI in North Australasia, supporting information Figure S1b). We therefore propose that a combined influence of climate patterns contributes to the observed regional atmospheric CO IAV. Variability over the time periods of maximum variability (September to December, see Figure 3) are modeled in section 4, using a combination of climate indices as explanatory variables.

4. Relationship Between CO Variability and Climate

4.1. Regression Methodology

We use multiple linear regression to model the relationship between month average climate mode indices and CO month average anomalies, using stepwise forward and backward variable selection to determine the final model with best predictive power. Statistical models are developed using MATLAB and our analysis tools are publicly available on the MATLAB Central File Exchange (<https://www.mathworks.com/matlabcentral/fileexchange/68319-southern-hemisphere-carbon-monoxide-modeling>). The Bayesian information criterion (BIC) is used as the selection criteria, due to it being well suited for predictive purposes (e.g., Faraway, 2014). BIC penalizes models that contain more variables over models with fewer variables, thereby counteracting an implicitly improved fit due to an increased number of variables. All combinations of the four climate indices with lags between 1 and 8 months are tested, where each model can at most contain one lagged version of each climate index. We found no major secondary peak in the partial autocorrelation plots for each climate mode (not shown), which suggests that including only one lag will capture most of the variability. Therefore, we choose only one lag for this analysis, but future research could analyze the difference between multiple lags of one climate mode index compared to the models found here. Lags of zero are not considered because our aim was to develop models with predictive properties for future applications. The maximum lag of 8 months was determined from single-variable lagged correlation analysis between indices and CO anomalies (see supporting information Figure S1). Most regions showed largest-magnitude correlations below 8 months, apart from TSA in Maritime SEA and Central Southern Africa, which showed a correlation peak with CO at 9 months, as well as Niño3.4 and DMI in Central South America, which show correlations peaks at 9 and 11 months, respectively. The 8-month maximum was chosen as a compromise between capturing the variability and increasing the likelihood of finding models by chance from testing too many models. This setup results in $8^4 = 4,096$ combinations of the four climate indices for each region. For comparison, the number of models to test by adding in a second lag for each climate mode would be $8^4 \times 7^4 = 9,834,496$, vastly increasing the probability of finding a seemingly good model by chance. The highest-order terms in our models are first-order interaction terms, which can be interpreted as the effect of one climate mode depending on the state of the other, resulting in a multiplicative cross term. It is a reasonable assumption to include interaction of climate modes due to the connectivity of the climate system. For each combination of climate indices we determine the model with the best model from among these models using the highest adjusted R^2 .

For a given region, the general formula for a multiple linear regression model with first-order interaction terms is shown in equation (1):

$$\text{CO}_{\text{anomaly}}(t) = \mu + \sum_k a_k \cdot \chi_k(t - \tau_k) + \sum_{ij} b_{ij} \cdot \chi_i(t - \tau_i) \cdot \chi_j(t - \tau_j) \quad (1)$$

where μ is a constant mean displacement; a_k, b_{ij} are coefficients; k is between 1 and 4; χ are climate indices (summarized in Table 1); and τ is a lag of 1 to 8 months for each index. Note that not all climate indices need be included in this equation and in that case, k may be less than 4. Additionally, once selected, the τ is the same for main effects and interaction terms. Fitting CO anomalies as opposed to concentrations removes

Table 2

Determined Lag Values (τ_k , Months), Coefficient Values and Model Fit Statistics for the Best Predictive Model of September to December CO Anomalies for Each Region, Between 2001 and 2016

Climate mode	Maritime SEA	Australasia		Southern Africa		South America	
		North	South	Central	South	Central	South
τ_k							
Niño 3.4	1	3	7	7	8	8	8
DMI	8	1	1	4	4	6	1
TSA	5	7	2	2	2	2	2
SAM	1	1	8	2	2	2	5
μ							
Constant	-0.29 (0.23)	-0.35 (0.16)	0.05 (0.11)	-0.09 (0.13)	0.04 (0.10)	-0.13 (0.25)	-0.06 (0.09)
χ_k							
a_k							
Niño 3.4	1.15 (0.26)	0.31 (0.31)	1.45 (0.23)	1.86 (0.30)	1.71 (0.24)	3.14 (0.45)	1.17 (0.17)
DMI	0.67 (0.64)	1.34 (0.23)	0.9 (0.19)	0.79 (0.30)	1.085 (0.31)	3.07 (0.81)	1.19 (0.18)
TSA	0.70 (0.72)	-1.10 (0.42)	-1.86 (0.49)	-1.00 (0.68)	-0.98 (0.66)	-4.84 (1.22)	-0.73 (0.40)
SAM	0.33 (0.27)	-0.19 (0.16)	-0.48 (0.14)	0.40 (0.13)	0.18 (0.13)	0.03 (0.24)	-0.05 (0.09)
$\chi_i \times \chi_j$							
b_{ij}							
Niño 3.4×DMI	-4.81 (0.77)	1.55 (0.40)	NS	NS	0.73 (0.35)	2.68 (1.10)	NS
Niño 3.4×TSA	NS	-2.75 (0.79)	-2.73 (0.73)	-2.26 (0.93)	-3.65 (0.79)	-7.60 (1.42)	-1.72 (0.54)
Niño 3.4×SAM	NS	NS	NS	NS	NS	-1.01 (0.29)	-0.49 (0.16)
DMI×TSA	-5.83 (1.94)	NS	NS	2.88 (1.45)	NS	NS	NS
DMI×SAM	NS	NS	NS	NS	NS	NS	-0.69 (0.19)
TSA×SAM	-2.88 (0.94)	-1.29 (0.53)	NS	NS	2.97 (0.72)	4.45 (1.42)	NS
Model fit statistics							
R^2	0.75	0.72	0.60	0.51	0.62	0.65	0.63
Adjusted R^2	0.72	0.69	0.56	0.46	0.57	0.60	0.58
RMSE ($\times 10^{17}$)	1.59	0.95	0.82	1.04	1.03	1.84	0.66
ENSO-only R^2	0.52	0.36	0.18	0.24	0.19	0.13	0.08

Note. Standard errors are shown in parentheses. Coefficient values (μ , a_k , b_{ij}) are scaled by $\times 10^{17}$. Selected model statistics are also shown. R^2 is a measure of variability explained with 1 being variability completely explained, Adjusted R^2 disadvantages models with a higher number of variables, RMSE = root-mean-square error between measured and modeled CO anomalies, ENSO-only R^2 relates to single-variable correlation between Niño 3.4 and CO anomalies in each region. NS = not selected; SEA = Southeast Asia; DMI = Dipole Mode Index; TSA = Tropical South Atlantic; SAM = Southern Annular Mode; ENSO = El Niño – Southern Oscillation.

the necessity to model seasonality. The lack of a trend term is discussed below in section 4.2. Finally, if interaction terms are present, then main effects associated with the interactions are necessary.

4.2. Best Predictive Models

Using the procedure described in section 4.1, we determine the model with best predictive power for each region. Resulting time lags and coefficient values that regionally fit equation (1) are shown in Table 2. It is not valid to directly compare the magnitudes of model coefficients between regions because different combinations of indices describe different regions. That is, models for each region must be interpreted as the combination of all terms. However, comparison can be made across regions for the lag values, the presence or absence of terms and the fitting statistics.

Time lags are interpreted as climate mode indices leading the CO anomalies. Optimum lag values found by stepwise regression are not necessarily the same as the optimum lag from single-value cross correlation (supporting information Figure S1) because multilinear fitting removes redundant information—thus accounting for correlation between climate modes. Results indicate that Niño 3.4 leads CO anomalies with low time lags for Maritime SEA and North Australasia compared to other regions (Table 2), reflecting the strong and direct connection to ENSO phases. In contrast, TSA displays longer lead times in Maritime SEA and North Australasia, compared to 2 months in other regions. This suggests a delayed influence of TSA on either transported CO

or on teleconnections to local climate responses. Lead times for DMI are variable, and SAM generally displays low lead times, apart from in South Australasia, where SAM leads CO anomalies by 8 months.

Our selected models require the use of all climate mode indices to explain CO variability. Additionally, all the models include interaction terms (Table 2), which are found to add a substantial amount of explanatory power. Selecting the best predictive models from a set that includes interaction terms resulted in an R^2 at least 0.1 points higher compared to selecting from a set without interaction terms (not shown). All possible combinations of interaction terms occur at least once in our analysis, with the most recurrent across regions being Niño 3.4×TSA—present everywhere except for Maritime SEA.

Generally, over 50% of variability is explained by the models, with over 70% for Maritime SEA and North Australasia, reflecting that atmospheric CO in these regions has a strong connection to climate (Table 2). The adjusted R^2 values account for intrinsically improved fitting that occurs when including more variables (e.g., Faraway, 2014) and are between 0.03 and 0.05 points lower than R^2 . If we equivalently use only the ENSO index at optimum time lag to predict CO anomalies over the same time period, we find substantially lower R^2 (0.55 to 0.23 points lower, last row of Table 2) than our models that include multiple climate indices and interaction terms.

Maritime SEA displays the highest R^2 value of all modeled regions (0.75, adjusted R^2 0.72), indicating the majority of CO variability in this region can be explained by the climate modes in the Southern Hemisphere and tropics. The fit in this region seems to be better in the later record after 2010 compared to before, a property that is not found in the other regions. Linear models tend to the mean, and the later record is less variable, so would be expected to form a better fit. The cause of higher variability in the earlier record may be due to changing sources of CO, but chemical transport modeling would be required to attribute the exact cause.

Although we only show one best model in Table 2, we record the top three models, rated by adjusted R^2 , for Maritime SEA in the supporting information (Table S1 and Figure S5). BIC only slightly differs between the three models, and lags are almost equivalent, only changing by 1 month for one index between different models. Small changes in lags are expected due to the broad peaks of correlation found in single-value correlation analysis (supporting information Figure S1), which indicate that a range of similar lags may have similar skill. The three best models also give the same combination of interaction terms, with little difference in coefficient values, indicating that the *best model* results are robust. Similar results are found for the other regions.

The South Australasia region is represented by the most simple model, including only one interaction term Niño 3.4×TSA. CO at South Australian sites has been found to be relatively more influenced by transported fire emissions from South America and Southern Africa than the North Australian sites, with North Australia experiencing more influence from local fire emissions (Buchholz et al., 2016). Therefore, this interaction term in South Australasia could be a reflection of transported emissions. In comparison, the North Australasia model includes Niño 3.4×DMI and TSA×SAM in addition to the Niño 3.4×TSA interaction term.

Moderate R^2 values for most of the regions indicate missing explanatory variables, particularly for the region with the lowest value: Central Southern Africa ($R^2 = 0.51$). This region experiences transport from North Africa and is close to the transport from emissions due to cropland expansions (Andela & van der Werf, 2014), which would therefore experience a human-driven variability not necessarily driven by climate variability. Also, possible biogenic contributions to CO may have counteracting variability patterns not captured in this analysis (Marais et al., 2014).

The greatest number of interaction terms occurs for Central South America, with four combinations required, suggesting many contributions to CO variability. However, the moderate R^2 indicates some explanation of variability is missing. In this case we may need to include the climate mode Atlantic Multi-decadal Oscillation (AMO), as that is known to be related to rainfall in the Amazon region (Aragão et al., 2007), as well as burned area (Chen et al., 2016). There may also be a missing human component of emissions from deforestation activities (Chen et al., 2013; Tang & Arellano, 2017) that involves felling biomass followed by drying and subsequent burning. Although the main amount of burning from this human component would occur in the dry season and the dryness of fuel would be related to climate responses, the amount of biomass available to burn (and consequently emissions) would not necessarily be related to climate. Additionally, our chosen regions could be too large and potentially encompass counteracting modes of variability (Holz et al., 2012).

Modeled and measured anomaly time series are plotted in Figure 4. The models generally reproduce the anomaly maxima and minima. However, it is clear that the models underperform in some years. Specifically,

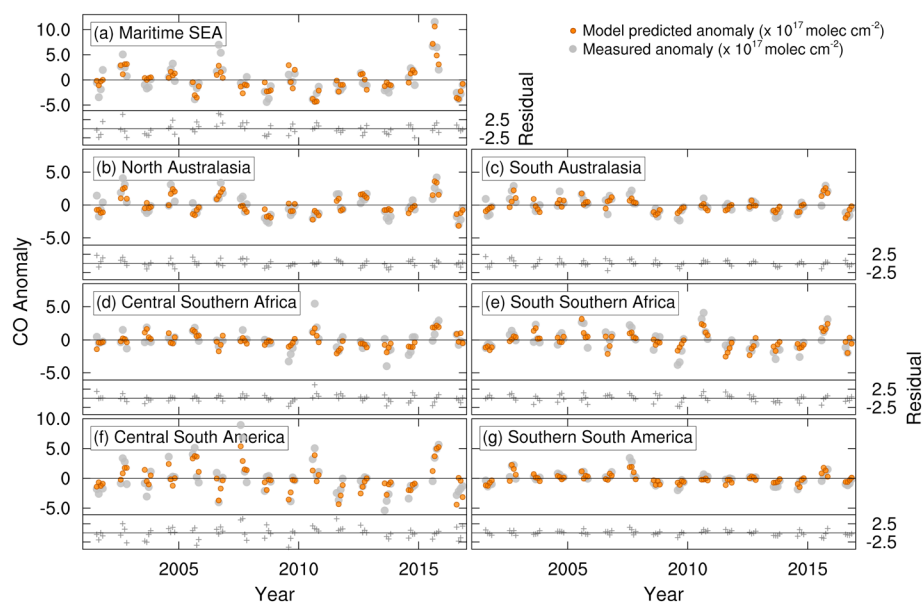


Figure 4. Measured and model predicted CO anomalies for September to December in the studied regions between 2001 and 2016. Residual shows the difference between the two data sets (measured value-modeled value). SEA = Southeast Asia.

the 2006 maximum in Maritime SEA and 2007 maximum in Central South America is not well captured. Models for both of the Southern African regions have difficulty reproducing the magnitude of 2009 and 2010 anomalies. Poor skill in these years could be explained by alternative responses to climate in these regions. Therefore, future analysis of a time-varying climate relationship may help explain more variability.

Measurement-model residuals do not indicate any need for a model term to account for a trend or systematic bias. Although global background CO has been found to show a trend of approximately -1% per year (Worden et al., 2013), the anomaly data sets developed here show no trend. We find that accounting for any trend in the fitting algorithm did not improve statistics for the selected best model. A lack of a significant CO trend in our analysis is most likely due to focusing on biomass burning source regions, where large variability in sources masks any trend signal. Strode and Pawson (2013) found that more than 20 years of measurements are required to determine a 3% per year magnitude trend over biomass burning regions, and consequently, a longer time period would be required here to determine a smaller magnitude trend of -1% per year. Future analysis with longer time series may need to revisit CO trends.

4.3. Forward Prediction Capability for Maritime SEA

Predicting atmospheric composition in Maritime SEA has the potential to provide early warning about air quality hazards that could assist in prevention of health consequences. For example, studies of the air pollution from 2015 biomass burning in this region found severe impacts on human health (Crippa et al., 2016; Koplitz et al., 2016). We assess predictive capability of our technique by determining the coefficients in the Maritime SEA region using CO anomalies and climate indices between 2001 and 2014. Subsequently, the

resulting model is applied to climate index values for 2015 and 2016 in order to predict CO anomalies for these years. We find the best predictive model for 2001–2014 using the methodology described in section 4.1, apart from lags being set to those determined in section 4.2.

Even without including the 2015 and 2016 data during fitting, the resulting model is very similar to the selected best Maritime SEA model from section 4.2 and is able to predict the peak CO anomaly in 2015 to within 20% of the measured value and the 2016 minimum anomaly to within 7% (Figure 5). These anomalies are predicted with a 1-month lead time. Coefficient of variation for the predicted data (2015–2016) is 0.97, with mean bias of -3% , relative to the measurements. This indicates that the statistical model developed here has potential to be used as an operational

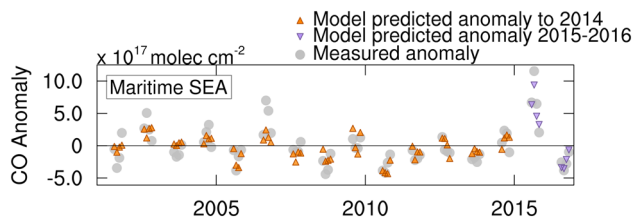


Figure 5. Measured and model predicted CO anomalies in Maritime SEA. Model was trained using 2001–2014 measured CO anomalies and subsequently applied to 2015–2016 climate indices (indicated by different icons). Note that the modeled values are slightly different to those in Figure 4. SEA = Southeast Asia.

prediction tool to forecast CO loading, which can be used as a proxy for fire emissions in air quality models for the Maritime SEA region. Future research will include assessing the robustness of predictability by random selection of training and test data. Limiting the lags to longer lead times will also be investigated to determine the longest viable lead time. In addition to future CO prediction, the model will be applied to past measured climate modes, which span decades, consequently providing insight for recent changes in regional atmospheric composition.

5. Discussion of Potential Causality

We have shown that the statistical methodology applied has predictive capabilities for atmospheric CO variability. However, a limitation of this method is that the resulting models describe a relationship but do not imply causality. The physical action of the link between climate modes and atmospheric composition may be through the influence of climate on processes that affect both local and distant emissions, as well as transport pathways. In order to disentangle these processes and attribute causality, global chemical transport modeling along with a similar climate index regression analysis is required and is the subject of future research. However, here we compare our results to previous findings in order to gain insight into how our models relate to causal effects.

There is a strong relationship between biomass burning and CO in our regions of study, so we expect that climate-burned area relationships will be a component of climate-CO relationships. Chen et al. (2016) performed linear regression analyses between ocean climate indices and a $1^\circ \times 1^\circ$ grid of burned area to produce coherent regions where similar model parameters were found, with a maximum of two variables in their resulting models. Their method further differed from ours in that they used single-variable correlation to set the lag and climate mode index of the first variable, thereby essentially fitting the residual with second variable, with some flexibility. In general, they found that nonlinear combinations produced better correlations than linear combinations of the same model, supporting our finding of the benefit of interaction terms. We consequently use the two-variable models of Chen et al. (2016) to interpret our interaction terms.

Chen et al. (2016) found that Pacific and Indian Ocean climate indices were important for Maritime SEA and North Australasia, which is consistent with our results. This suggests that when limiting regression model terms to two, the Pacific and Indian Oceans provide the greatest influence for these regions. Chen et al. (2016) findings also suggest that the combination of these two ocean terms in our models (Niño 3.4×DMI) mainly influences local burning emissions. In comparison, our South Australasian region does not include the Indian and Pacific Ocean interaction term, reflecting that this region is mainly influenced by transported emissions from regions other than Maritime SEA or North Australasia.

The only relevant region from Chen et al. (2016) for Africa is a subportion of our Central Southern Africa region, where they found that the Indian and Atlantic Oceans are important, suggesting our DMI×TSA influences local burning. In our Central South America region, Chen et al. (2016) found three subregions with separate coherent model parameters, which may be the reason we find such a complicated model in our analysis. The Indian, Atlantic, and Pacific Oceans were all important for influencing burning in the Amazon (Chen et al., 2016). Apart from the southwest Amazon region where the AMO was important, Chen et al. (2016) found that Southern Hemisphere ocean basins had the major influence on areas within our study regions, supporting our choice of climate mode indices. The relatively low explanation of variability in our model for the South American regions could therefore be due to omitting the AMO index from our analysis.

Overall, our best fit models include more terms than Chen et al. (2016), which reflects that variability in CO loading is driven by more than just burned area within each region. Study of atmospheric loading complements burned area and fire emission studies by also accounting for transported sources. The benefit of predicting CO anomalies directly provides a link to complete air quality responses, intrinsically including changes in transported sources of CO. In contrast, fire products must be converted into emissions using emission factors (which can be quite uncertain) and subsequently used in regional or global models to interpret spatial coverage and transported contributions. Consequently, both CO anomalies and the resulting statistical models found here can be used to test climate-chemistry models, potentially providing insight into sources of model error.

6. Conclusion

Our study investigates an aspect of the coupling between chemistry and climate. Specifically, we analyze a 16-year record of total column CO from the satellite instrument MOPITT and find that IAV is within a similar range for all investigated regions of the Southern Hemisphere and tropics. The connection to climate is determined by systematically developing explanatory models between climate mode indices and CO anomalies, with the goal of predicting future CO loading during the fire season.

We analyze the ability of indices for four climate modes (ENSO, IOD, TSA, and AAO), chosen to represent the major oceans of the Southern Hemisphere and tropics, to reproduce variability in atmospheric CO loading. We find that climate modes can be used to predict CO anomalies. Using stepwise forward and backward variable selection with BIC to identify the optimal regression models between climate indices and CO anomalies, we find different results for the seven regions of interest (Maritime SEA, plus two subregions in each of Australasia, Southern Africa, and South America). Generally, over 50% of variability can be explained by the climate modes in all regions and above 70% in the tropical regions of Maritime SEA and North Australasia. Moderate explanation of variability in the other regions is likely be a symptom of missing explanatory variables. Future studies that: include an index describing the human-driven component (such as cropland or deforestation dynamics), use a moving climate-CO relationship, and/or include the AMO climate mode index for the South American regions, may improve the ability of our models to represent CO variability. With the future addition of more explanatory variables, we are also interested in relaxing the lag values to greater than 1 month, in order to find the maximum possible lead time for predicting CO anomalies with confidence. Recent atmospheric composition changes outside of the current satellite CO record will also be explored by applying the models to past climate modes.

A unique aspect of our analysis is testing for optimum climate mode interactions. We find that first-order interaction terms of the climate modes are necessary when explaining CO variability. In all our models, interaction terms are required, with at least one first-order interaction term in every region. This indicates the importance of interactions between different climate modes in driving atmospheric composition responses.

We also assess the predictive power for the Maritime SEA region and find good predictability, indicating a potential for use in forecasting air quality in the region. Since these predictions intrinsically include changes in transported sources of CO, they also inform air quality responses to climate-driven fires.

Acronyms

AAO	Antarctic Oscillation
ASEAN	Association of Southeast Asian Nations
AMO	Atlantic Multi-decadal Oscillation
BIC	Bayesian information criterion
CAM-chem	Community Atmosphere Model with Chemistry
DMI	Dipole Mode Index (climate mode index for the Indian Ocean Dipole)
ENSO	El Niño–Southern Oscillation
IOD	Indian Ocean Dipole
IAV	Interannual variability
MERRA	Modern-Era Retrospective Analysis for Research Applications
MOPITT	Measurements Of Pollution In The Troposphere (satellite instrument measuring carbon monoxide)
NCAR	National Center for Atmospheric Research
NOAA	National Oceanic and Atmospheric Administration
SAM	Southern Annular Mode (Climate mode index for the Antarctic Oscillation)
SEA	Southeast Asia
TIR	Thermal infrared
TSA	Tropical South Atlantic (climate mode index for the South Atlantic Ocean)

Acknowledgments

The National Center for Atmospheric Research (NCAR) is sponsored by the National Science Foundation (NSF). Any opinions, findings, and conclusions or recommendations expressed in the publication are those of the author(s) and do not necessarily reflect the views of the NSF. The NCAR MOPITT project is supported by the National Aeronautics and Space Administration (NASA) Earth Observing System (EOS) program. MOPITT products are publicly available through several repositories linked via <http://terra.nasa.gov/about/terra-instruments/mopitt> or <https://www2.acom.ucar.edu/mopitt>. MOPITT anomaly data can be found at NCAR's Research Data Archive (RDA): <https://rda.ucar.edu/datasets/ds682.0>. Datasets used in and tools developed for the analyses are available on the MATLAB Central File Exchange: <https://www.mathworks.com/matlabcentral/fileexchange/68319-southern-hemisphere-carbon-monoxide-modeling>. Thank you to Peter Simonson and Lewis Blake who helped develop the code release. We thank Chi-Fan Shih for assistance with the RDA data set submission. We wish to thank the MOPITT team at NCAR, Boulder, Colorado, USA, for data processing and algorithm support. MOPITT instrument operations were supported by the MOPITT team at the University of Toronto, Ontario, Canada. The MOPITT team also acknowledges support from the Canadian Space Agency (CSA), the Natural Sciences and Engineering Research Council (NSERC), and Environment Canada, and the contributions of COMDEV (the prime contractor) and ABB BOMEM. We are grateful to NOAA for producing and supplying climate index data, which is publicly available at <https://stateoftheocean.osmc.noaa.gov> and <http://www.cpc.ncep.noaa.gov>. We thank Elizabeth Asher and Sara Martínez-Alonso for their valuable suggestions.

References

Andela, N., & van der Werf, G. R. (2014). Recent trends in African fires driven by cropland expansion and El Niño to La Niña transition. *Nature Climate Change*, 4(9), 791–795. <https://doi.org/10.1038/nclimate2313>

Andreoli, R. V., & Kayano, M. T. (2006). Tropical Pacific and South Atlantic effects on rainfall variability over Northeast Brazil. *International Journal of Climatology*, 26(13), 1895–1912. <https://doi.org/10.1002/joc.1341>

Aragão, L. E. O. C., Malhi, Y., Roman-Cuesta, R. M., Saatchi, S., Anderson, L. O., & Shimabukuro, Y. E. (2007). Spatial patterns and fire response of recent Amazonian droughts. *Geophysical Research Letters*, 34, L07701. <https://doi.org/10.1029/2006GL028946>

Aragão, L. E. O. C., & Shimabukuro, Y. E. (2010). The incidence of fire in Amazonian forests with implications for REDD. *Science*, 328(5983).

Arellano, A., Hess, P., Edwards, D., & Baumgardner, D. (2010). Constraints on black carbon aerosol distribution from Measurement of Pollution in the Troposphere (MOPITT) CO. *Geophysical Research Letters*, 37, L17801. <https://doi.org/10.1029/2010GL044416>

Austin, K. G., González-Roglich, M., Schaffer-Smith, D., Schwantes, A. M., & Swenson, J. J. (2017). Trends in size of tropical deforestation events signal increasing dominance of industrial-scale drivers. *Environmental Research Letters*, 12(5), 054009. <https://doi.org/10.1088/1748-9326/aa6a88>

Australian Bureau of Statistics (2016). Retrieved from <http://www.abs.gov.au/AUSSTATS/abs@nsf/mf/3101.0>

Bamston, A. G., Chelliah, M., & Goldenberg, S. B. (1997). Documentation of a highly ENSO-related SST region in the equatorial Pacific: Research note. *Atmosphere-Ocean*, 35(3), 367–383. <https://doi.org/10.1080/07055900.1997.9649597>

Bhardwaj, P., Naja, M., Kumar, R., & Chandola, H. C. (2016). Seasonal, interannual, and long-term variabilities in biomass burning activity over South Asia. *Environmental Science and Pollution Research*, 23(5), 4397–4410. <https://doi.org/10.1007/s11356-015-5629-6>

Bian, H., Chin, M., Kawa, S. R., Yu, H., Diehl, T., & Kucsera, T. (2010). Multiscale carbon monoxide and aerosol correlations from satellite measurements and the GOCART model: Implication for emissions and atmospheric evolution. *Journal of Geophysical Research*, 115, D07302. <https://doi.org/10.1029/2009JD012781>

Bloom, A. A., Worden, J., Jiang, Z., Worden, H., Kurosu, T., Frankenberg, C., & Schimel, D. (2015). Remote-sensing constraints on South America fire traits by Bayesian fusion of atmospheric and surface data. *Geophysical Research Letters*, 42, 1268–1274. <https://doi.org/10.1002/2014GL02584>

Bowman, K. P. (2006). Transport of carbon monoxide from the tropics to the extratropics. *Journal of Geophysical Research*, 111, D02107. <https://doi.org/10.1029/2005JD006137>

Bowman, D. M. J. S., Balch, J., Artaxo, P., Bond, W. J., Cochrane, M. A., D'Antonio, C. M., et al. (2011). The human dimension of fire regimes on Earth. *Journal of Biogeography*, 38(12), 2223–2236. <https://doi.org/10.1088/1748-9326/aa6a88>

Bryan, B. A., Nolan, M., McKellar, L., Connor, J. D., Newth, D., Harwood, T., et al. (2016). Land-use and sustainability under intersecting global change and domestic policy scenarios: Trajectories for Australia to 2050. *Global Environmental Change*, 38, 130–152. <https://doi.org/10.1016/j.gloenvcha.2016.03.002>

Buchholz, R. R., Deeter, M. N., Worden, H. M., Gille, J., Edwards, D. P., Hannigan, J. W., et al. (2017). Validation of MOPITT carbon monoxide using ground-based Fourier transform infrared spectrometer data from NDACC. *Atmospheric Measurement Techniques*, 10(5), 1927–1956. <https://doi.org/10.5194/amt-10-1927-2017>

Buchholz, R., Paton-Walsh, C., Griffith, D., Kubistin, D., Caldow, C., Fisher, J., et al. (2016). Source and meteorological influences on air quality (CO, CH₄ & CO₂) at a Southern Hemisphere urban site. *Atmospheric Environment*, 126, 274–289. <https://doi.org/10.1016/j.atmosenv.2015.11.041>

Chen, Y., Morton, D. C., Andela, N., Giglio, L., & Randerson, J. T. (2016). How much global burned area can be forecast on seasonal time scales using sea surface temperatures? *Environmental Research Letters*, 11(4), 45001. <https://doi.org/10.1088/1748-9326/11/4/045001>

Chen, Y., Morton, D. C., Jin, Y., Collatz, G. J., Kasibhatla, P. S., van der Werf, G. R., et al. (2013). Long-term trends and interannual variability of forest, savanna and agricultural fires in South America. *Carbon Management*, 4(6), 617–638. <https://doi.org/10.4155/cmt.13.61>

Cleverly, J., Eamus, D., Luo, Q., Restrepo Coupe, N., Kljun, N., Ma, X., & other (2016). The importance of interacting climate modes on Australia's contribution to global carbon cycle extremes. *Scientific Reports*, 6, 23113. <https://doi.org/10.1038/srep23113>

Costafreda-Aumedes, S., Comas, C., & Vega-García, C. (2017). Human-caused fire occurrence modelling in perspective: A review. *International Journal of Wildland Fire*, 26(12), 983. <https://doi.org/10.1071/WF17026>

Crippa, P., Castruccio, S., Archer-Nicholls, S., Lebron, G. B., Kuwata, M., Thota, A., et al. (2016). Population exposure to hazardous air quality due to the 2015 fires in equatorial Asia. *Scientific Reports*, 6(1), 37074. <https://doi.org/10.1038/srep37074>

Davidson, E. A., de Araújo, A. C., Artaxo, P., Balch, J. K., Brown, I. F., Bustamante, M. M. C., et al. (2012). The Amazon basin in transition. *Nature*, 481(7381), 321–328. <https://doi.org/10.1038/nature10717>

Deeter, M. N., Edwards, D. P., Francis, G. L., Gille, J. C., Martínez-Alonso, S., Worden, H. M., & Sweeney, C. (2017). A climate-scale satellite record for carbon monoxide: The MOPITT version 7 product. *Atmospheric Measurement Techniques*, 10, 2533–2555. <https://doi.org/10.5194/amt-10-2533-2017>

Deeter, M. N., Edwards, D. P., Gille, J. C., & Drummond, J. R. (2007). Sensitivity of MOPITT observations to carbon monoxide in the lower troposphere. *Journal of Geophysical Research*, 112, D24306. <https://doi.org/10.1029/2007JD008929>

Deeter, M. N., Emmons, L. K., Francis, G. L., Edwards, D. P., Gille, J. C., Warner, J. X., et al. (2003). Operational carbon monoxide retrieval algorithm and selected results for the MOPITT instrument. *Journal of Geophysical Research*, 108, 4399. <https://doi.org/10.1029/2002JD003186>

Deeter, M. N., Martínez-Alonso, S., Edwards, D. P., Emmons, L. K., Gille, J. C., Worden, H. M., et al. (2014). The MOPITT version 6 product: Algorithm enhancements and validation. *Atmospheric Measurement Techniques*, 7(11), 3623–3632. <https://doi.org/10.5194/amt-7-3623-2014>

Edwards, D. P., Emmons, L. K., Gille, J. C., Chu, A., Attié, J. L., Giglio, L., et al. (2006). Satellite observed pollution from Southern Hemisphere biomass burning. *Journal of Geophysical Research*, 111, D14312. <https://doi.org/10.1029/2005JD006655>

Edwards, D. P., Emmons, L. K., Hauglustaine, D. A., Chu, D. A., Gille, J. C., Kaufman, Y. J., et al. (2004). Observations of carbon monoxide and aerosols from the Terra satellite: Northern Hemisphere variability. *Journal of Geophysical Research*, 109, D24202. <https://doi.org/10.1029/2004JD004727>

Edwards, D. P., Pétron, G., Novelli, P. C., Emmons, L. K., Gille, J. C., & Drummond, J. R. (2006). Southern Hemisphere carbon monoxide interannual variability observed by Terra Measurement of Pollution in the Troposphere (MOPITT). *Journal of Geophysical Research*, 111, D16303. <https://doi.org/10.1029/2006JD007079>

Emmons, L. K., Edwards, D. P., Deeter, M. N., Gille, J. C., Campos, T., Nédélec, P., et al. (2009). Measurements of Pollution in the Troposphere (MOPITT) validation through 2006. *Atmospheric Chemistry and Physics*, 9(5), 1795–1803. <https://doi.org/10.5194/acp-9-1795-2009>

Enfield, D. B., Mestas-Núñez, A. M., Mayer, D. A., & Cid-Serrano, L. (1999). How ubiquitous is the dipole relationship in tropical Atlantic sea surface temperatures? *Journal of Geophysical Research*, 104(C4), 7841–7848. <https://doi.org/10.1029/1998JC900109>

- Fanin, T., & van der Werf, G. R. (2017). Precipitation–fire linkages in Indonesia (1997–2015). *Biogeosciences*, 14(18), 3995–4008. <https://doi.org/10.5194/bg-14-3995-2017>
- Faraway, J. J. (2014). *Linear Models with R, Second Edition*. Boca Raton, FL: CRC Press, Taylor & Francis Group LLC.
- Field, R. D., van der Werf, G. R., Fanin, T., Fetzer, E. J., Fuller, R., Jethva, H., et al. (2016). Indonesian fire activity and smoke pollution in 2015 show persistent nonlinear sensitivity to El Niño-induced drought. *Proceedings of the National Academy of Sciences of the United States of America*, 113(33), 9204–9209. <https://doi.org/10.1073/pnas.1524888113>
- Field, R. D., van der Werf, G. R., & Shen, S. S. P. (2009). Human amplification of drought-induced biomass burning in Indonesia since 1960. *Nature Geoscience*, 2(3), 185–188. <https://doi.org/10.1038/ngeo443>
- GlouDEMANS, A. M. S., KROL, M. C., MEIRINK, J. F., DE LAAT, A. T. J., VAN DER WERF, G. R., SCHRIJVER, H., et al. (2006). Evidence for long-range transport of carbon monoxide in the Southern Hemisphere from SCIAMACHY observations. *Geophysical Research Letters*, 33, L16807. <https://doi.org/10.1029/2006GL026804>
- Hendon, H. H., Thompson, D. W. J., Wheeler, M. C., Hendon, H. H., Thompson, D. W. J., & Wheeler, M. C. (2007). Australian rainfall and surface temperature variations associated with the Southern Hemisphere annular mode. *Journal of Climate*, 20(11), 2452–2467. <https://doi.org/10.1175/JCLI4134.1>
- Holz, A., Kitzberger, T., Paritsis, J., & Veblen, T. T. (2012). Ecological and climatic controls of modern wildfire activity patterns across southwestern South America. *Ecosphere*, 3(11), 1–25. <https://doi.org/10.1890/ES12-00234.1>, art103.
- Jiang, Z., Worden, J. R., Worden, H., Deeter, M., Jones, D. B. A., Arellano, A. F., & Henze, D. K. (2017). A 15-year record of CO emissions constrained by MOPITT CO observations. *Atmospheric Chemistry and Physics*, 17(7), 4565–4583. <https://doi.org/10.5194/acp-17-4565-2017>
- Kalnay, E., Kanamitsu, M., Kistler, R., Collins, W., Deaven, D., Gandin, L., et al. (1996). The NCEP/NCAR 40-year reanalysis project. *Bulletin of the American Meteorological Society*, 77(3), 437–471. [https://doi.org/10.1175/1520-0477\(1996\)077<0437:TNYRP>.0.CO;2](https://doi.org/10.1175/1520-0477(1996)077<0437:TNYRP>.0.CO;2)
- Kistler, R., Collins, W., Saha, S., White, G., Woollen, J., Kalnay, E., et al. (2001). The NCEP–NCAR 50-year reanalysis: Monthly means CD-ROM and documentation. *Bulletin of the American Meteorological Society*, 82(2), 247–267. [https://doi.org/10.1175/1520-0477\(2001\)082<0247:TNNYRM>2.3.CO;2](https://doi.org/10.1175/1520-0477(2001)082<0247:TNNYRM>2.3.CO;2)
- Kopplitz, S. N., Mickley, L. J., Marlier, M. E., Buonocore, J. J., Kim, P. S., Liu, T., et al. (2016). Public health impacts of the severe haze in equatorial Asia in September–October 2015: demonstration of a new framework for informing fire management strategies to reduce downwind smoke exposure. *Environmental Research Letters*, 11(9), 94023. <https://doi.org/10.1088/1748-9326/11/9/094023>
- Lamarque, J.-F., Emmons, L. K., Hess, P. G., Kinnison, D. E., Tilmes, S., Vitt, F., et al. (2012). CAM–chem: Description and evaluation of interactive atmospheric chemistry in the Community Earth System Model. *Geoscientific Model Development*, 5, 369–411. <https://doi.org/10.5194/gmd-5-369-2012>
- Langmann, B., Duncan, B., Textor, C., Trentmann, J., & van der Werf, G. R. (2009). Vegetation fire emissions and their impact on air pollution and climate. *Atmospheric Environment*, 43(1), 107–116. <https://doi.org/10.1016/j.atmosenv.2008.09.047>
- MOPITT Science Team (2013). MOPITT/Terra Level 2 CO vertical profiles derived from thermal infrared radiances, version 7, USA:NASA Atmospheric Science Data Center (ASDC), Hampton, VA. https://doi.org/10.5067/TERRA/MOPITT/MOP02T_L2.007
- Marais, E. A., Jacob, D. J., Guenther, A., Chance, K., Kurosu, T. P., Murphy, J. G., et al. (2014). Improved model of isoprene emissions in Africa using Ozone Monitoring Instrument (OMI) satellite observations of formaldehyde: Implications for oxidants and particulate matter. *Atmospheric Chemistry and Physics*, 14(15), 7693–7703. <https://doi.org/10.5194/acp-14-7693-2014>
- Marengo, J. A., Espinoza, J. C., & Extreme seasonal droughts and floods in amazonia: Causes, trends and impacts (2016). *International Journal of Climatology*, 36(3), 1033–1050. <https://doi.org/10.1002/joc.4420>
- Pumphrey, H. C., Santee, M. L., Livesey, N. J., Schwartz, M. J., & Read, W. G. (2011). Microwave Limb Sounder observations of biomass-burning products from the Australian bush fires of February 2009. *Atmospheric Chemistry and Physics*, 11(13), 6285–6296. <https://doi.org/10.5194/acp-11-6285-2011>
- Reddington, C. L., Butt, E. W., Ridley, D. A., Artaxo, P., Morgan, W. T., Coe, H., & Spracklen, D. V. (2015). Air quality and human health improvements from reductions in deforestation-related fire in Brazil. *Nature Geoscience*, 8(10), 768–771. <https://doi.org/10.1038/ngeo2535>
- Reynolds, R. W. (1988). A real-time global sea surface temperature analysis. *Journal of Climate*, 1(1), 75–87. [https://doi.org/10.1175/1520-0442\(1988\)001<0075:ARTG5S>2.0.CO;2](https://doi.org/10.1175/1520-0442(1988)001<0075:ARTG5S>2.0.CO;2)
- Reynolds, R. W., & Marsico, D. C. (1993). An improved real-time global sea surface temperature analysis. *Journal of Climate*, 6(1), 114–119. [https://doi.org/10.1175/1520-0442\(1993\)006<0114:AIRTGS>2.0.CO;2](https://doi.org/10.1175/1520-0442(1993)006<0114:AIRTGS>2.0.CO;2)
- Reynolds, R. W., Rayner, N. A., Smith, T. M., Stokes, D. C., & Wang, W. (2002). An improved in situ and satellite SST analysis for climate. *Journal of Climate*, 15, 1609–1625.
- Rienecker, M. M., Suarez, M. J., Gelaro, R., Todling, R., Bacmeister, J., Liu, E., et al. (2011). MERRA: NASA's Modern-Era Retrospective Analysis for Research and Applications. *Journal of Climate*, 24, 3624–3648. <https://doi.org/10.1175/JCLI-D-11-00015.1>
- Rodgers, C. D. (2000). *Inverse Methods for Atmospheric Sounding, Theory and Practice*. New Jersey: World Scientific Publishing Co. Ptd Ltd.
- Russell-Smith, J., Yates, C. P., Whitehead, P. J., Smith, R., Craig, R., Allan, G. E., et al. (2007). Bushfires 'down under': Patterns and implications of contemporary Australian landscape burning. *International Journal of Wildland Fire*, 16, 361–377. <https://doi.org/10.1071/WF07018>
- Saji, N. H., Goswami, B. N., Vinayachandran, P. N., & Yamagata, T. (1999). A dipole mode in the tropical Indian Ocean. *Nature*, 401(6751), 360–363. <https://doi.org/10.1038/43854>
- Saji, N., & Yamagata, T. (2003). Possible impacts of Indian Ocean Dipole mode events on global climate. *Climate Research*, 25(2), 151–169. <https://doi.org/10.3354/cr025151>
- Stavrakou, T., Müller, J.-F., Bauwens, M., De Smedt, I., Van Roozendaal, M., Guenther, A., et al. (2014). Isoprene emissions over Asia 1979–2012: Impact of climate and land-use changes. *Atmospheric Chemistry and Physics*, 14(9), 4587–4605. <https://doi.org/10.5194/acp-14-4587-2014>
- Strode, S. A., & Pawson, S. (2013). Detection of carbon monoxide trends in the presence of interannual variability. *Journal of Geophysical Research: Atmospheres*, 118, 12,257–12,273. <https://doi.org/10.1002/2013JD020258>
- Tang, W., & Arellano, A. F. (2017). Investigating dominant characteristics of fires across the Amazon during 2005–2014 through satellite data synthesis of combustion signatures. *Journal of Geophysical Research: Atmospheres*, 122, 1224–1245. <https://doi.org/10.1002/2016JD025216>
- Thompson, D. W. J., & Wallace, J. M. (2000). Annular modes in the extratropical circulation. Part I: Month-to-month variability. *Journal of Climate*, 13(5), 1000–1016. [https://doi.org/10.1175/1520-0442\(2000\)013<1000:AMITEC>2.0.CO;2](https://doi.org/10.1175/1520-0442(2000)013<1000:AMITEC>2.0.CO;2)
- van der Werf, G. R., Randerson, J. T., Giglio, L., Gobron, N., & Dolman, A. J. (2008). Climate controls on the variability of fires in the tropics and subtropics. *Global Biogeochemical Cycles*, 22(3), GB3028. <https://doi.org/10.1029/2007GB003122>

- Voulgarakis, A., Marlier, M. E., Faluvegi, G., Shindell, D. T., Tsigaridis, K., & Mangeon, S. (2015). Interannual variability of tropospheric trace gases and aerosols: The role of biomass burning emissions. *Journal of Geophysical Research: Atmospheres*, *120*, 7157–7173. <https://doi.org/10.1002/2014JD022926>
- Voulgarakis, A., Savage, N. H., Wild, O., Braesicke, P., Young, P. J., Carver, G. D., & Pyle, J. A. (2010). Interannual variability of tropospheric composition: The influence of changes in emissions, meteorology and clouds. *Atmospheric Chemistry and Physics*, *10*(5), 2491–2506. <https://doi.org/10.5194/acp-10-2491-2010>
- Wespes, C., Hurtmans, D., Clerbaux, C., & Coheur, P.-F. (2017). O₃ variability in the troposphere as observed by IASI over 2008–2016: Contribution of atmospheric chemistry and dynamics. *Journal of Geophysical Research: Atmospheres*, *122*, 2429–2451. <https://doi.org/10.1002/2016JD025875>
- Wespes, C., Hurtmans, D., Emmons, L. K., Safieddine, S., Clerbaux, C., Edwards, D. P., & Coheur, P.-F. (2016). Ozone variability in the troposphere and the stratosphere from the first 6 years of IASI observations (2008–2013). *Atmospheric Chemistry and Physics*, *16*(9), 5721–5743. <https://doi.org/10.5194/acp-16-5721-2016>
- Worden, H. M., Deeter, M. N., Frankenberg, C., George, M., Nichitiu, F., Worden, J., et al. (2013). Decadal record of satellite carbon monoxide observations. *Atmospheric Chemistry and Physics*, *13*, 837–850.
- Yin, Y., Ciais, P., Chevallier, F., van der Werf, Fanin, Broquet, G., et al. (2016). Variability of fire carbon emissions in equatorial Asia and its non-linear sensitivity to El Niño. *Geophysical Research Letters*, *43*, 10,472–10,479. <https://doi.org/10.1002/2016GL070971>
- Zhang, L., Jacob, D. J., Bowman, K. W., Logan, J. A., Turquety, S., & Hudman, R. C. (2006). Ozone-CO correlations determined by the TES satellite instrument in continental outflow regions. *Geophysical Research Letters*, *33*, L18804. <https://doi.org/10.1029/2006GL026399>

Erratum

In the originally published version of this article, AMO is incorrectly defined in the acronyms list. It should be defined as Atlantic Multi-Decadal Oscillation instead of Atlantic Meridional Oscillation. This error has since been corrected and this version may be considered the authoritative version of record.